Article

Challenging the ideal strength limit in single-crystalline gold nanoflakes through phase engineering

Tong Zhang [1,4], Yuanbiao Tong[2,4], Chenxinyu Pan[2], Jun Pei [1], Xiaomeng Wang[1], Tao Liu[1], Binglun Yin [1,3] ✉, Pan Wang [2] ✉, Yang Gao [1,3] ✉, Limin Tong [2] & Wei Yang [1,3]

Materials usually fracture before reaching their ideal strength limits. Meanwhile, materials with high strength generally have poor ductility, and vice versa. For example, gold with the conventional face-centered cubic (FCC) phase is highly ductile while the yield strength ($\sim 10^2$ MPa) is significantly lower than its ideal theoretical limit. Here, through phase engineering, we show that defect-free single-crystalline gold nanoflakes with the hexagonal close-packed (HCP) phase can exhibit a strength of 6.0 GPa, which is beyond the ideal theoretical limit of the conventional FCC counterpart. The lattice structure is thickness-dependent and the FCC-HCP phase transformation happens in the range of 11–13 nm. Suspended-nanoindentations based on atomic force microscopy (AFM) show that the Young's modulus and tensile strength are also thickness-and phase- dependent. The maximum strength is reached in HCP nanoflakes thinner than 10 nm. First-principles and molecular dynamics (MD) calculations demonstrate that the mechanical properties arise from the unconventional HCP structure as well as the strong surface effect. Our study provides valuable insights into the fabrication of nanometals with extraordinary mechanical properties through phase engineering.

Enhancing the strength of materials to their ideal theoretical limits has long been a challenging goal in scientific communities[1–8]. Meanwhile, fabricating materials with both high strength and high ductility is another long-term dilemma, due to the well-known conflict between strength and ductility[9–14]. Microstructure and external geometry are two essential factors, especially when the dimension of materials is down to the nanoscale[15–20]. Solid gold, usually holding the FCC phase, is highly ductile owing to its abundant slip systems and low generalized stacking fault energy[21,22], while displaying a rather low strength of $\sim 10^2$ MPa[23]. It has been widely reported that the strength of FCC gold can be dramatically improved by reducing its dimension[24,25]. Recently, gold nanosheets with the thickness around 50 nm were fabricated and

reported to possess a satisfactory strength of 1.2 GPa[26]. Microstructural strategies such as nanoscale twinning, have been integrated into the fabrication of gold nanowires with high strengths. For instance, ultrahigh-density twins (UDTs) with Å-scale have been reported to significantly hinder dislocation motions and even turn gold nanowires into brittle-like materials, reaching a near-ideal theoretical strength of FCC gold with ≈ 3.12 GPa[27], positioning gold among the roster of the strongest metals. On the other hand, HCP metals such as titanium or cobalt[28], generally exhibit substantially high strengths[29], due to their fewer and less easily activated slip systems, compared to FCC metals. In the past few decades, phase engineering strategies, such as phase transformation between conventional and

[1]Center for X-mechanics, Department of Engineering Mechanics, Zhejiang University, Hangzhou, China. [2]State Key Laboratory of Extreme Photonics and Instrumentation, College of Optical Science and Engineering, Hangzhou, China. [3]Key Laboratory of Soft Machines and Smart Devices of Zhejiang Province, Zhejiang University, Hangzhou, China. [4]These authors contributed equally: Tong Zhang, Yuanbiao Tong. ✉e-mail: binglun.yin@zju.edu.cn; nanopan@zju.edu.cn; ygao96@zju.edu.cn

unconventional phases, have been widely adopted for fabricating nanomaterials with distinct physical properties[17]. Therefore, a question naturally arises: can we explore the possibility of further enhancing the strength of gold and even reaching its ideal theoretical limit, in the unconventional HCP phase? In fact, the fabrication of HCP gold square sheets grown on graphene oxide has been reported in literature[30]. However, the mechanical properties of HCP gold yet remain unexplored.

Here, we report the investigation of the mechanical properties of single-crystalline gold nanoflakes with the unconventional HCP phase, by suspended-nanoindentation using atomic force microscopy. Following a wet-chemical method, we fabricated freestanding gold nanoflakes with thicknesses ranging from 5 to 34 nm and a lateral size of ≈50 μm. The lattice structure as well as the high quality (single-crystalline and defect-free) of the nanoflakes were revealed by high-resolution transmission electron microscopy (HRTEM). Particularly, the ideal theoretical strength of FCC gold (5.5 GPa) is experimentally surpassed in HCP gold nanoflakes thinner than 10 nm, with a tensile strength of 6.0 GPa[5,27]. In addition, our gold nanoflakes are purely brittle when the thickness is less than 10 nm. Clear ductile fracture behavior emerges in nanoflakes thicker than 10 nm while retaining a lower yet considerably high strength of 2–3 GPa. The underlying mechanisms of the exceptional mechanical properties of the HCP gold nanoflakes are unveiled by first-principle calculations based on density functional theory (DFT). This material system contains rich phenomena and complex phase transformation at the nanoscale, offering valuable insights for the design and fabrication of metal nanostructures with extraordinary mechanical properties.

Results

Phase-engineered single-crystalline gold nanoflakes

Freestanding gold nanoflakes thicker than 10 nm were first fabricated using a modified wet-chemical approach[31]. The thickness can be tuned from ≈10 nm to hundreds of nanometers by controlling the growth time. As depicted in the schematic of Fig. 1a–c, the gold nanoflakes with thickness less than 10 nm were obtained by an atomic-level precision etching approach on the as-fabricated thick nanoflakes with cysteamine solution (see Methods)[32]. The thickness can be precisely controlled by the etching time. Figure 1d–i presents the optical images of the fabricated gold nanoflakes with thicknesses of 32, 16, and 6 nm, respectively. With the decrease in the thickness, the reflection of gold nanoflakes decreases, while the transmission increases gradually. The uniform thinning technique enabled us to fabricate gold nanoflakes with highly controllable thickness and atomically flat surface. An AFM topographic image of a 5.7 nm-thick gold nanoflake and its corresponding height profile are displayed in Fig. 1j, k, respectively. The surface roughness of the gold nanoflake is less than 0.5 nm, confirming the atomic flatness.

HRTEM experiments were performed to investigate the lattice structures of the gold nanoflakes. Figure 2a, d shows the HRTEM images of an 11.7 nm-thick nanoflake and a 13.7 nm-thick nanoflake, respectively. The two images were captured along the thickness direction, both showing uniform and completely defect-free hexagonal lattice structures (with 6-fold symmetry), indicating that the atomic close-packed planes are perpendicular to the thickness direction[31,32]. It is worth noting that both the projected {0001} plane of an HCP crystal and the projected {111} plane of an FCC crystal exhibit hexagonal lattice structures[33,34]. However, the distances between the nearest edge-on atomic planes for the two nanoflakes are rather different, as shown in Fig. 2b, e—zoom-in regions in Fig. 2a, d, respectively. To be specific, the interplanar spacing of 0.25 nm in Fig. 2b matches the theoretical value for HCP lattice structure viewing along the <0001> beam direction[32–35], while the interplanar spacing of 0.15 nm in Fig. 2e matches the theoretical value for FCC lattice structure viewing along the <111> beam direction[31,34,35] (see more discussions on the lattice structure identification in Suppl. Note 1). The HCP phase in Fig. 2a can be further evidenced by the selected area electron diffraction (SAED) pattern in Fig. 2c. The diffraction spot sets exhibit a
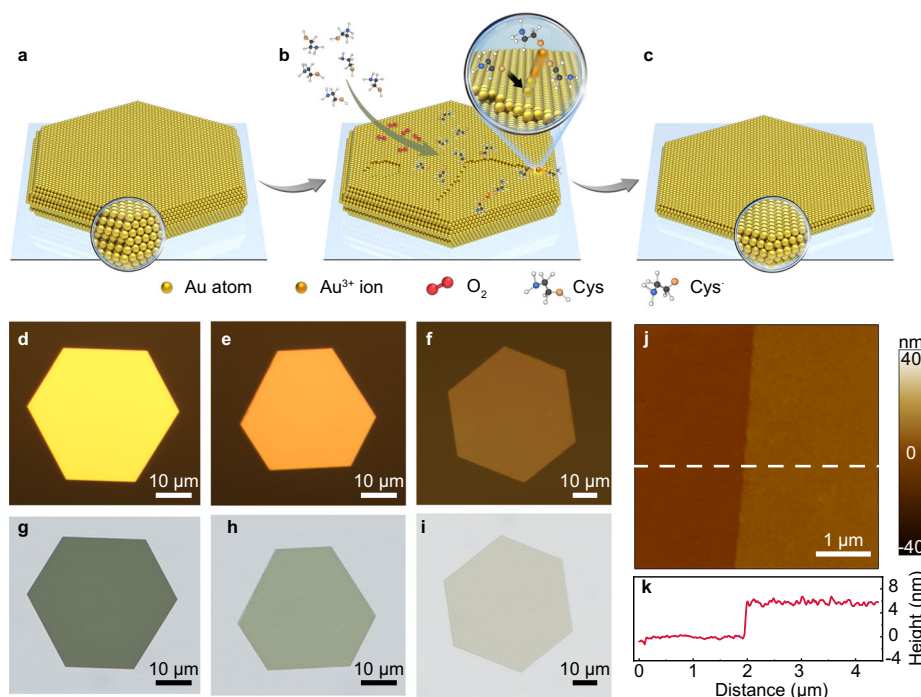

Fig. 1 | Fabrication and basic characterizations of single-crystalline gold nanoflakes. a–c Schematic of the fabrication of single-crystalline gold nanoflakes, which transformed from **a**, the FCC phase to **c**, the HCP phase during the thinning process. Cys, cysteamine. Cys•, cysteamine radical. **d–i** Reflection and transmission optical images of gold nanoflakes, corresponding to the thickness of (**d**, **g**), 32 nm, (**e**, **h**), 16 nm, and (**f**, **i**), 6 nm, respectively. **j** AFM topographic image of a 5.7 nm-thick gold nanoflake and **k**, its corresponding height profile (red solid line), source data are provided as a Source Data file.
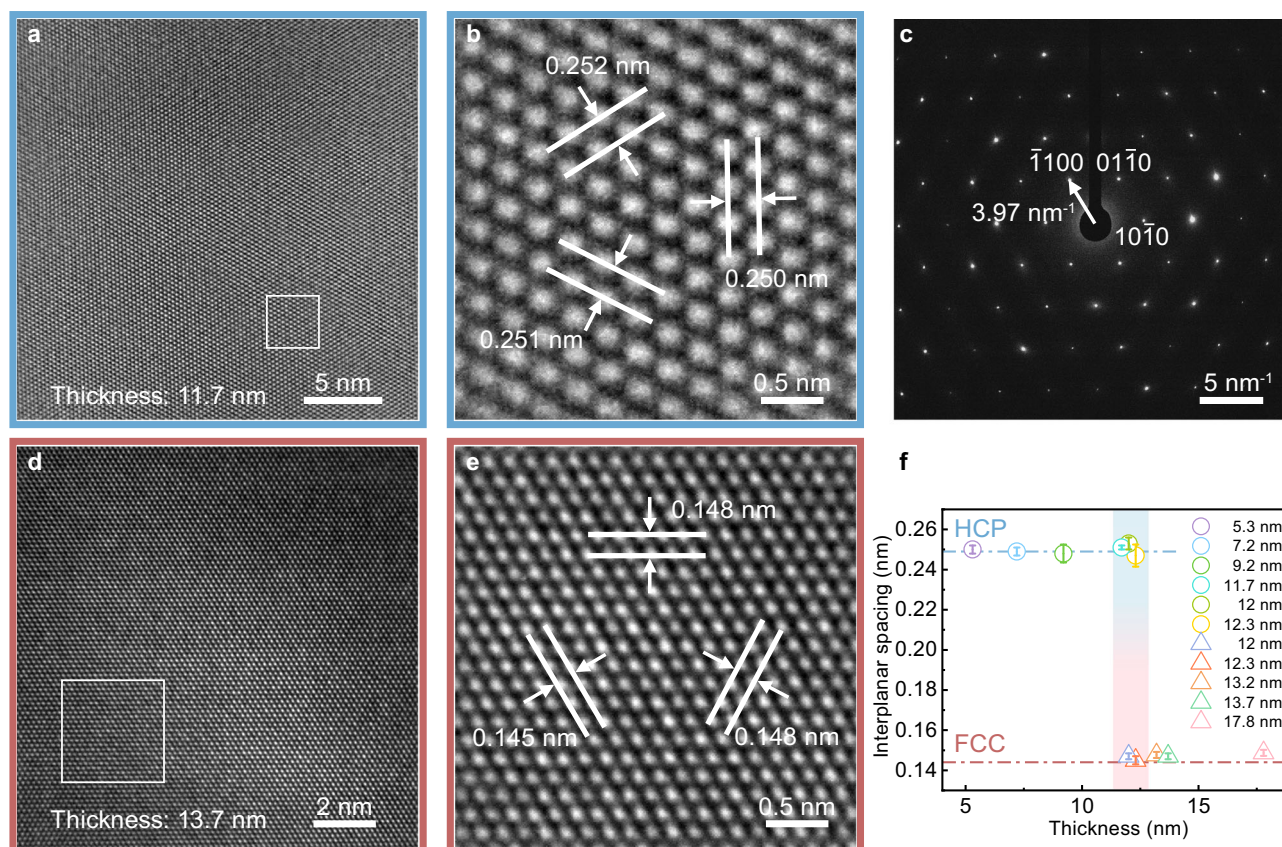
Fig. 2 | HRTEM characterizations along the thickness direction. a HRTEM image of a random area in an 11.7 nm-thick gold nanoflake showing hexagonal lattice structures (highlighted by a blue frame). **b** HRTEM image of a zoom-in region in **a**, where the distance between the nearest edge-on atomic planes is ≈0.25 nm (highlighted by a blue frame). **c** SAED pattern corresponding to **a**, matching HCP structure viewing along the <0001> beam direction. **d** HRTEM image of a random area in a 13.7 nm-thick gold nanoflake displaying hexagonal lattice structures (highlighted by a red frame). **e** HRTEM image of a zoom-in region in **d**, revealing a distance of ≈0.15 nm between the nearest edge-on atomic planes (highlighted by a red frame), corresponding to FCC structure viewing along the <111> beam direction. **f** Statistical analysis of the interplanar spacing in gold nanoflakes with different thicknesses. Error bars represent standard deviations for at least 6 independent measurements for each sample. Blue dotted line, the theoretical value (0.249 nm) of the interplanar spacing of HCP lattice structure viewing along the <0001> beam direction. Red dotted line, the theoretical value (0.144 nm) of the interplanar spacing of FCC lattice structure viewing along the <111> beam direction. The gradient color bar (from blue to red) indicates the phase transformation range, source data are provided as a Source Data file.

6-fold symmetry, with the reciprocal lattice vector magnitude of 3.97 nm^{-1}, matching the HCP structure viewing along the <0001> beam direction[35]. The above results confirm the existence of both HCP and FCC phases in our gold nanoflakes, similar to a previous study by Huang et al., wherein the lattice structure of the gold square sheets undergoes a transformation from HCP to FCC at a critical thickness of ≈2.4 nm[30]. Moreover, the gold nanoflakes in this work could maintain pure and stable HCP phase (the lattice structure remained completely unchanged throughout several HRTEM experiments on the same nanoflake) when the thickness is at least ≈11 nm, which are the thickest HCP gold nanoflakes ever reported. Figure 2f displays the statistics of the interplanar spacing observed along the thickness direction of gold nanoflakes with various thicknesses. The data points in Fig. 2f can be clearly divided into two groups, corresponding to the HCP (blue dotted line) and the FCC (red dotted line) lattice structures, respectively. Based on Fig. 2f, we can easily identify an FCC-to-HCP phase transformation in the range of 11–13 nm (see more HRTEM images in Suppl. Note 2). Therefore, phase engineering of our gold nanoflakes can be delicately achieved by simply tuning the thickness. HCP phase was never observed in all the HRTEM characterizations for those gold nanoflakes thicker than 15 nm[31] (Suppl. Figs. 2 and 3), meaning the FCC-to-HCP phase transformation is driven during the chemical etching process. DFT calculations reveal that FCC phase is the ground state for bulk gold, while the energy gap between HCP- and FCC- phases is

significantly narrowed and the HCP phase becomes a metastable state, if the nanoflake thickness is reduced to a few nanometers. We also observed the fingerprints of the reverse HCP-to-FCC phase transformation triggered by focused ion beam (FIB), as shown in Suppl. Fig. 4. The DFT calculations and the phase transformation mechanism will be discussed later in the main text and Suppl. Notes 14, 15.

Mechanical experiments

To investigate the exceptional mechanical properties of the phase-engineered gold nanoflakes, we conducted nanoindentation measurements using an atomic force microscope[26,36], as depicted in the schematic of Fig. 3a. Gold nanoflakes with thicknesses ranging from 5 to 34 nm were first transferred onto silicon substrates with 4-μm holes using a water-assisted transfer method (see Methods). The typical AFM non-contact images of a transferred gold nanoflake are exhibited in Fig. 3b, indicating the flat intimate contact between the clamped gold nanoflake and the substrate without folding, forming a freestanding suspended structure. Then an AFM tip was placed at the center of the suspended gold nanoflake, followed by the sample stage moving upward at a constant displacement rate of 1 μm s^{-1} and sampling rate of 2 kHz. Several displacement rates were tested and no distinct difference was found (Suppl. Fig. 10). For each sample, consecutive loading/unloading cycles were implemented with an increasing applied force until the fracture of the nanoflake. To avoid possible damage or worn-
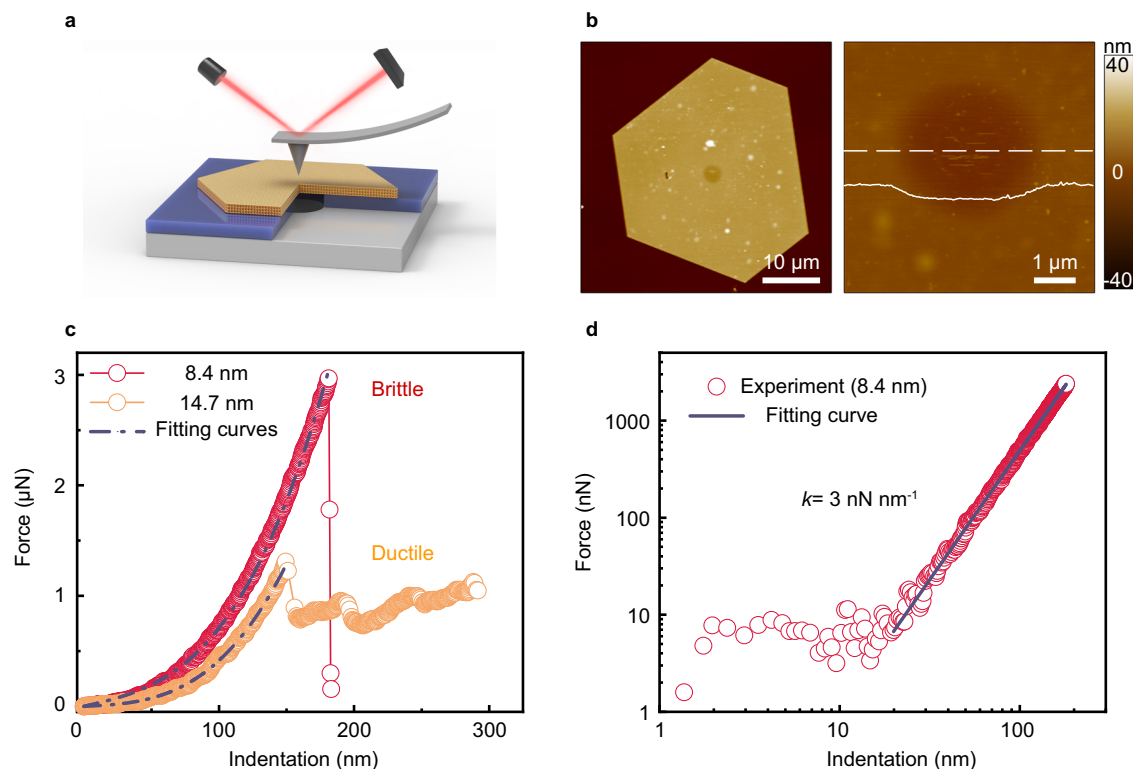
Fig. 3 | Nanoindentation measurements. a Schematic of the nanoindentation experiment on a suspended gold nanoflake. **b** AFM topographic images for a gold nanoflake transferred onto a 4-μm hole. White solid line, the height profile marked by the white dashed line. **c** Representative indentation curves for gold nanoflakes with the dashed lines showing the fitting curves following Eq. (1). Red circle, the indentation curve for an 8.4 nm-thick nanoflake, showing brittle behavior. Orange circle, the indentation curve for a 14.7 nm-thick nanoflake, showing ductile behavior. **d** Indentation curve for the 8.4 nm-thick gold nanoflake in logarithmic scale, indicating a clear cubic behavior for high loads. Source data are provided as a Source Data file.

out which may change the shapes or radii of AFM tips during successive experiments, diamond coated AFM tips were used, whose radii and cantilever spring constants were thoroughly calibrated (see Methods and Suppl. Note 5). The loading curves for the same nanoflake coincide quite well with each other, revealing high data accuracy and excellent elastic behavior before fracture. No slippery was detected according to the AFM topographic images before and after the indentation. Figure 3c displays two representative force-indentation curves for gold nanoflakes with the thicknesses of 8.4 and 14.7 nm, respectively. More indentation curves can be found in Suppl. Note 7. The force-indentation relationship at the midpoint of a circular clamped nanoflake can be modeled as follows[36,37]:

$$F = \left[\frac{4\pi E}{3(1-v^2)} \cdot \left(\frac{t^3}{R^2}\right)\right]\delta + (\pi T)\delta + \left(\frac{q^3 E t}{R^2}\right)\delta^3, \quad (1)$$

where F is the applied force, δ is the central indentation of the nanoflake, t is the thickness of the nanoflake which was scrupulously identified in AFM contact mode. R is the hole radius, T is the prestress related to the transfer process and surface state of the suspended nanoflake, E is the Young's modulus of the nanoflake and v is the Poisson's ratio adopted as 0.42, q is a dimensionless constant which relates to Poisson's ratio, such that $q = 1/(1.05 - 0.15v - 0.16v^2)$. Since the Poisson's ratio of HCP gold has not been reported in literature, we tested different values ranging from 0.40 to 0.49. The corresponding Young's modulus and the strength fluctuate by only 7.9% and 4%, respectively (detailed result in Suppl. Table 1). Therefore, we use a Poisson's ratio of 0.42 without significant loss of accuracy. The first term in Eq. (1) represents a linear bending plate behavior dominating the small-load regime. The third term in Eq. (1) represents a nonlinear

membrane stretching behavior, characterized by a cubic relationship between F and δ, which dominates when the load is large. A representative indentation curve of the 8.4 nm-thick gold nanoflake is replotted in a logarithmic scale in Fig. 3d. The indentation curve exhibits a nearly perfect cubic $F \approx \delta^3$ relationship for almost the whole indentation (from ≈20 to 160 nm), indicating that stretching is the dominant deformation over bending in the indentation experiments. More details on the supporting theories are in Suppl. Note 6. For all the gold nanoflakes we tested, Eq. (1) fits the indentation curves very well ($R^2 > 0.99$), as shown in Fig. 3c and Suppl. Fig. 8. Through two-parameter curve fitting, we can obtain the Young's modulus and the prestress of the tested gold nanoflake. The influence of hole size on nanoindentation experiments is discussed in Suppl. Fig. 9. The tensile strength is then calculated using the maximum force F_{frac} in the indentation curves, using Eq. (2)[38]:

$$\sigma = \sqrt{\frac{F_{frac}E}{4\pi t r_{tip}}}. \quad (2)$$

The Young's modulus and tensile strength of the gold nanoflake are plotted as a function of the thickness in Fig. 4. In a wide range of thickness, the Young's modulus is above 100 GPa, indicating the high quality of the nanoflakes. Moreover, both the Young's modulus and the tensile strength increase significantly with the reduction of the thickness, displaying explicit thickness dependence. It's worth noting that the Young's modulus increases continuously with the decrease in thickness, while the strength shows a ≈2 GPa jump across the thickness range for the FCC-to-HCP transformation. This distinction possibly arises from the co-existence of the FCC/HCP phases in those
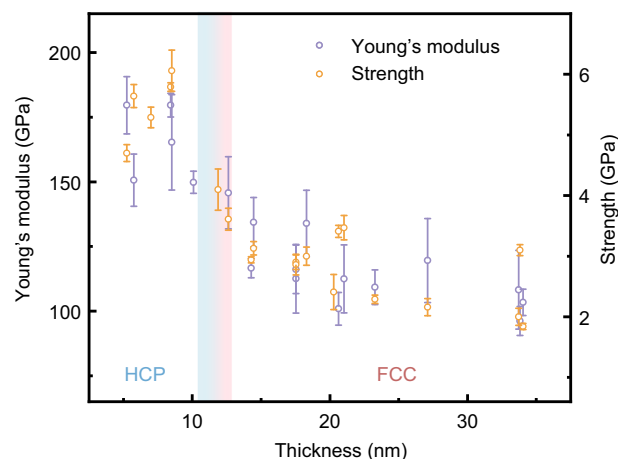
Fig. 4 | Experimental Young's modulus and strength of the phase-engineered gold nanoflakes. Both the Young's modulus (purple points) and the strength (orange points) increase significantly with the decrease in thickness, during which the gold nanoflakes transform from FCC phase into HCP phase. The gradient color bar (from blue to red) indicates the HCP-to-FCC phase transformation range. Error bars represent standard deviations obtained from 5–18 independent measurements for each sample. Source data are provided as a Source Data file.
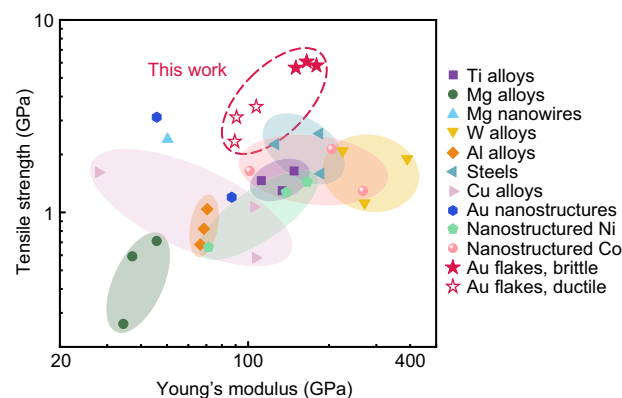

Fig. 5 | Comparison of the ultimate tensile strength and Young's modulus of the phase-engineered HCP gold nanoflakes with those of other advanced nano-metals. The solid red stars correspond to the brittle gold nanoflakes with the highest strengths, and the hollow red stars correspond to the gold nanoflakes with relatively lower strengths and clear ductility. Other data points include Ti alloys (dark purple square)[29,62,63], Mg alloys (dark green circle)[64–66], Mg nanowires (light blue upward-pointing triangle)[9], W alloys (light orange downward-pointing triangle)[67–69], Al alloys (dark orange rhombus)[70–72], steels (cyan leftward-pointing triangle)[43,73,74], Cu alloys (light purple rightward-pointing triangle)[6,75,76], nanostructured Ni (light green pentagon)[77–79], nanostructured Co (pink sphere)[28,80,81] and some Au nanostructures (dark blue hexagon)[26,27].

nanoflakes whose thicknesses lie in the phase transformation range (more detailed discussion in Suppl. Note 13). The maximum tensile strength is 6.0 GPa, achieved in an 8.4 nm-thick nanoflake, and the corresponding indentation curve is plotted in Fig. 3c. It is noteworthy that the maximum strength in this study surpasses the theoretical yield strength of the conventional FCC gold (5.5 GPa)[5,27]. Besides, the gold nanoflakes with the thickness below 10 nm display a completely brittle fracture behavior, while ductile behavior emerges as the thickness increases. A representative indentation curve for a 14.7 nm-thick nanoflake is plotted in Fig. 3c, showing the absence of stage II work-hardening and clear discrete plasticity separated by several elastic loading segments, which can be explained by the dislocation starvation mechanism[39–41]. Due to the large surface-to-volume ratio and small thickness, mobile dislocations are more likely to annihilate at a nearby free surface rather than multiply within the gold nanoflakes. Moreover, the defect-free single-crystalline structure and atomically flat surface result in a scarcity of dislocation sources. Such a dislocation-starved state requires significantly high stresses to nucleate additional dislocations. It should be noted that those nanoflakes with clear ductility still possess a satisfactory strength of 2–3 GPa, exceeding most of other metals or alloys, as shown in Fig. 5. With the thickness further increasing, a typical stage II work-hardening curve was observed[42] (Suppl. Fig. 12). The brittle-ductile transition in our gold nanoflakes could be attributed to the emergence of FCC phase when the thickness increases. To better illustrate its exceptional mechanical properties, we plot the tensile strength and Young's modulus of the phase-engineered gold nanoflake with other advanced nanometals and alloys in Fig. 5. The Young's modulus of the HCP gold nanoflakes is comparable to those of the state-of-the-art titanium alloys and steels, while the maximum strength exceeds ≈94% and ≈136% of the state-of-the-art reported values for gold nanostructures (3.12 GPa)[27] and steels (2.57 GPa)[43], respectively.

DFT calculations

Compared to conventional FCC polycrystals[44], our phase-engineered single-crystalline gold nanoflakes exhibit exceptionally high Young's modulus, mainly in the HCP structure. In this section, we discuss and rationalize such observations based on linear elasticity[45] and DFT calculations[46]. In nanoindentation experiments, the main deformation of the nanoflakes is the in-plane biaxial tension applied by the AFM tip

(Suppl. Fig. 7). For any biaxial deformation in the x_1-x_2 plane, the general formalism of the stress-strain constitutive relation is:

$$\begin{bmatrix} \sigma_1 \\ \sigma_2 \\ 0 \\ 0 \\ 0 \\ \sigma_6 \end{bmatrix} = C_{ij} \begin{bmatrix} x \\ x \\ \varepsilon_3 \\ \varepsilon_4 \\ \varepsilon_5 \\ 0 \end{bmatrix}. \tag{3}$$

Here, x is the applied strain; σ_i (i = 1, 2, 6) and ε_i (i = 3, 4, 5) are the stress and strain components that arise due to the applied strain x and boundary conditions. Given the single-crystal elastic constants C_{ij}, these unknown components can be derived as a function of x. The elastic strain energy density ($\sigma_1 + \sigma_2$) $x/2$ can then be calculated and denoted as Ax^2, where the coefficient A describes the effective stiffness of the in-plane biaxial deformation, and is purely determined by the C_{ij} (see Suppl. Table 4). All the materials analyzed in the following are assumed to be transversely isotropic and have a constant in-plane Poisson's ratio of v = 0.42, which leads to the direct calculation of the in-plane modulus as (1-v) A.

The analyses start with the single-crystals of bulk FCC gold. The corresponding C_{ij} of FCC gold has been reported in Ref. 44, based on which the effective stiffness A in the {100} and {111} planes are calculated as 78 and 190 GPa, respectively. The corresponding in-plane moduli are 45 and 110 GPa, of which the average value (78 GPa) is very close to the polycrystal Young's modulus 79 GPa[44], as shown in Fig. 6a. This is reasonable as the polycrystal "stiffness" is a mixture of the "hard" and "soft" orientations. We then performed DFT calculations to verify the in-plane moduli of the {100} and {111} planes for FCC bulk, and the results are highly consistent with the experiments, as shown in Fig. 6a. Hence, even within the FCC bulk state, the in-plane modulus of the {111} plane for single-crystals is dramatically higher than the value for polycrystals. Next, we applied the same calculations on the HCP bulk state. As shown in Fig. 6a, the in-plane modulus of the HCP basal plane is 146 GPa, which is substantially higher than the FCC {111} value (110 GPa). Therefore, remaining in bulk states, the in-plane modulus for single-crystal HCP gold is higher than the value for FCC gold. Finally, we calculated the in-plane modulus for HCP structures with
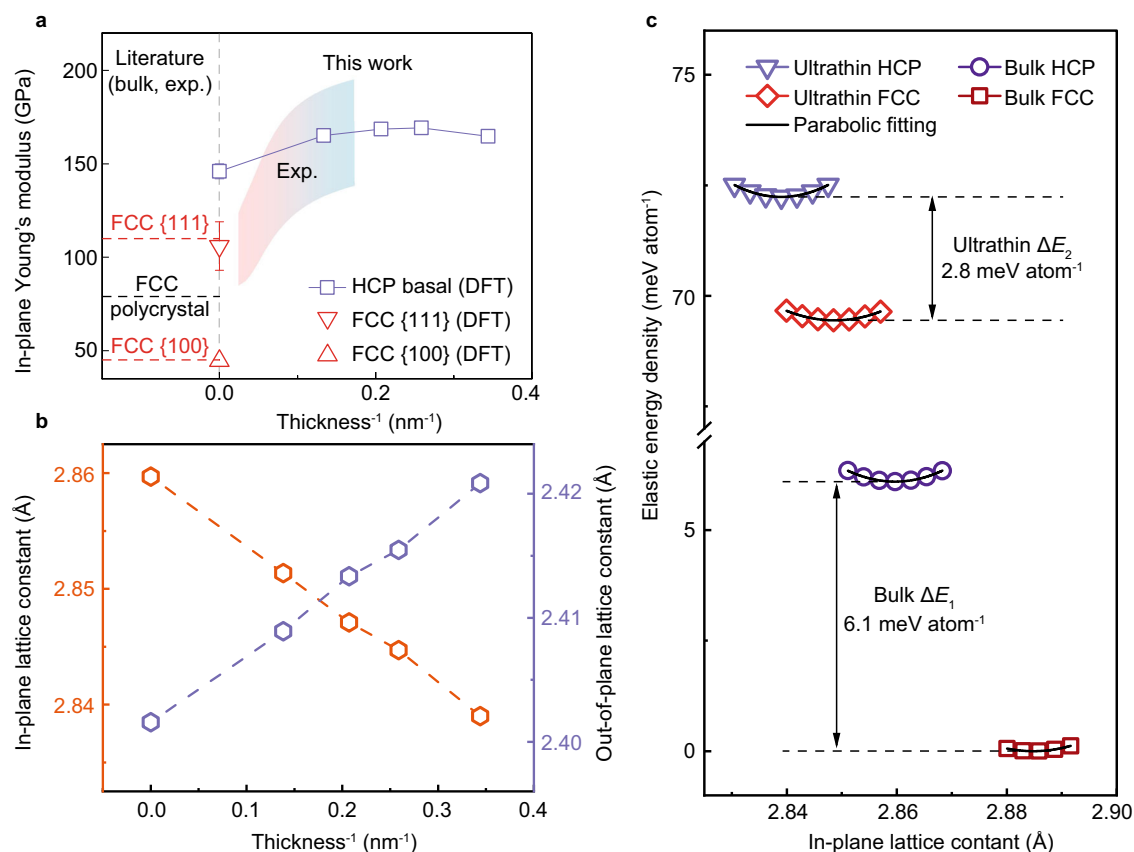
Fig. 6 | DFT calculations of the in-plane modulus, lattice constants and phase stability. a The in-plane Young's modulus of gold for various states. Black dashed line, Young's modulus of polycrystalline gold[47]. Red dashed lines, the in-plane moduli for bulk FCC {111} and {100} planes, derived from ref. 44. Red triangles, DFT-calculated in-plane moduli for bulk FCC {111} and {100} planes. Purple squares, the in-plane moduli for the HCP basal structure with various thicknesses. The experimental Young's modulus presented in Fig. 4 are replotted for comparison, as indicated by the gradient color bar from red (FCC phase) to blue (HCP phase). **b** The calculated in-plane (orange hexagon) and out-of-plane (purple hexagon) lattice constants of HCP gold with various thicknesses. **c** The formation energy of gold as a function of the in-plane lattice constant in biaxial deformation for various states. The black solid curves are the parabolic fittings. The energy reference is the FCC bulk state in equilibrium. For both bulk and ultrathin (12 atomic layers) cases, the energy differences between the HCP and FCC phases are highlighted with arrows. Purple triangle, ultrathin HCP state. Red rhombus, ultrathin FCC state. Dark purple circle, bulk HCP state. Dark red square, bulk FCC phase. Source data are provided as a Source Data file.

various thicknesses, ranging from 12 to 30 atomic layers. As shown in Fig. 6a, with the decrease in thickness, the in-plane modulus gets further enhanced and reaches the maximum value of ≈170 GPa at ≈4 nm (16 atomic layers), in excellent agreement with our AFM experiments (discussed in Fig. 4, replotted in Fig. 6a). We attribute the thickness-dependence of the in-plane modulus observed in both experiments and calculations to surface effect. The free surface naturally lies in a higher energy state and tends to shrink[47], leading to a smaller intrinsic in-plane lattice constant and a higher modulus than the interior body. The surfaces and the body are thus subjected to appropriate strains to overcome the lattice mismatch, resulting in a smaller overall in-plane lattice constant and a higher modulus than the bulk state, as shown in Fig. 6a, b. The surface effect usually gets more prominent as the dimension decreases, giving rise to the thickness dependence of the in-plane modulus. It's also worth noting that the calculated Young's modulus slightly decreases when the thickness decreases from 16 to 12 atomic layers. This is probably due to the fact that the two free surfaces start to interact, thus compromising the system stability. See Suppl. Note 14 for detailed modeling and discussions. Overall, the analyses here are consistent both theoretically and experimentally, revealing the mechanisms for the exceptional mechanical properties in the gold nanoflakes.

DFT calculations are also performed to unfold the physical origin of the thickness-dependent phase transformation. Figure 6c shows the

energy (per atom) as a function of the in-plane lattice constant in the biaxial deformation, where the energy vs. lattice constant curves are in excellent agreement with parabolic fitting. In Fig. 6c, the reference energy is the equilibrium energy of the FCC bulk state, which turns out to be the ground state of gold in DFT. The HCP bulk energy is higher than that of the ground FCC state by ≈6.1 meV atom^{-1}, consistent with the previous results in ref. 48. Then for the case with 12 atomic layers, the formation energy increases significantly (by ≈70 meV atom^{-1}) as compared to those in bulk due to the surface effect. More importantly, the energy difference between the ultrathin HCP and FCC states reduces significantly to 2.8 meV atom^{-1}, indicating that the HCP phase is more favored in the ultrathin scale than in the bulk. Another crucial observation is that the in-plane lattice constant in the HCP phase is considerably smaller than the value for the FCC phase (in both the bulk and ultrathin cases), which could explain why HCP gold is generally stiffer than FCC gold. In addition to examining the thickness effect, we also conducted preliminary calculations to investigate the substrate effect on the energy difference (see Suppl. Note 15 for more details). Based on all the DFT calculations performed, two key conclusions have been drawn. First, with decreasing thickness or in the presence of a substrate, the energy gap between the FCC- and HCP- phases is significantly reduced compared to the bulk state. Second, the FCC phase consistently exhibits a lower energy state compared to the HCP phase. These conclusions are in full agreement with experimental

observations, as elaborated below. During the chemical fabrication process, thinner gold nanoflakes have a higher probability to be in the HCP phase[30]. This observation aligns with the first conclusion that smaller thickness favors the HCP phase. Although the HCP phase has slightly higher energy, various external factors[17,33,40,49–52], such as chemical groups, thermal activation, and substrate effects, collectively enable the system to overcome the energy barrier and stabilize in the metastable HCP phase. Another experimental observation is that an HCP-to-FCC phase transformation occurs when sufficient thermal perturbation is applied to the nanoflakes. As shown in Suppl. Fig. 4, a significant number of stacking faults and ultrahigh-density twins were generated in a 7.6-nm-thick HCP nanoflake after exposure to gallium ion beams. Stacking faults and UDTs are reported to be the fingerprints of the intermediate state of the HCP-to-FCC transformation in gold. This strongly suggests that the FCC phase is energetically more favorable, which once again is consistent with the DFT results. The analyses here not only support the existence of the HCP phase observed in HRTEM but also reveal the possible mechanism for the transformations between the FCC- and HCP- phases.

Discussion

Based on the experiments and calculations, we attribute the high strength for the gold nanoflakes in this work to the defect-free HCP structure and the surface effect. First of all, HCP metals typically lack sufficient slip systems to release elastic strain energy through dislocation motions, and the critical resolved shear stress also varies significantly for different slip systems in HCP phase, thereby resulting in poor ductility and a high stress required to initiate relative movement between adjacent atomic planes[9]. In our suspended-nanoindentation experiments, biaxial loading is applied with the tensile direction perpendicular to the direction of the close-packed plane. According to previously reported DFT calculations[48], only 3 different {0001} < -1100> slip systems can be more easily activated in HCP gold, compared to other slip systems in the basal, prismatic, and pyramidal planes, making it quite difficult to accommodate sufficient plastic deformations. MD simulations were performed using the embedded atom method[53] to further understand the dynamics of dislocation nucleation and multiplication at the very early stage of deformations (Suppl. Fig. 17). As expected, 1/3{0001} < -1100> slip system is dominated until the fracture. In contrast, under the same loading conditions, at least 12 different {111} < 11-2> slip systems can be easily activated in FCC gold nanoflakes, resulting in distinct mechanical behaviors. Moreover, ultrahigh-density twins have been experimentally proven as an effective strategy to enhance the strength of metals by restricting dislocation motions[27]. Therefore, the "ABAB…" stacking in HCP gold can be intuitively approximated as FCC gold composed of ultrahigh-density twins with minimal twin thickness[17], resulting in the high strength. Secondly, the defect-free structure and the atomically flat surface significantly limit the dislocation nucleation in the early stage of deformations, intrinsically enhancing the strength of the gold nanoflakes. Meanwhile, the large surface-to-volume ratio gives rise to a pronounced surface effect, inducing certain compressive stress against the external tensile loading.

In summary, we report the fabrication of single-crystalline HCP gold nanoflakes with a high strength, which is even beyond the ideal theoretical strength of conventional FCC gold, as confirmed by nanoindentation measurements. The exceptional mechanical properties are attributed to a series of mechanisms including the unconventional HCP phase, surface effect and the absence of defects. Considerable ductility was also observed in thicker nanoflakes where the HCP and FCC phase might co-exist. This material system could serve as a platform to demonstrate the impacts of unconventional phases, external geometry and size effect on the mechanical properties of nanometals, and to investigate the very early stage of metal deformation and fracture. More importantly, this work offers an approach to resolve the conflict between strength and ductility by means of phase engineering.

Methods

Fabrication of gold nanoflakes
Gold nanoflakes with thicknesses larger than 10 nm were fabricated using a modified wet-chemical approach[31]. First, in a 20-mL glass vial, a growth solution was prepared by mixing a 90-μL chloroauric acid (≥99.9%) aqueous solution (0.1 M) with 10-mL ethylene glycol (≥99.5%). Then, a cleaned glass slide was inserted into the growth solution to serve as the substrate for the growth of gold nanoflakes. Finally, the growth solution was heated to 95 °C and kept at this temperature for a certain time, which defines the dimensions of the resulting gold nanoflakes. After the growth, the glass slide with gold nanoflakes on the surface was cleaned with ethanol (≥99.7%) and dried with nitrogen. For gold nanoflakes with thickness less than 10 nm, they were fabricated by an atomic-level-precision chemical etching approach of substrate-supported gold nanoflakes with cysteamine (≥98.0%) solution (200 mM in chloroform, ≥99.0%). Substrate-supported gold nanoflakes with thickness around 20 nm were immersed into the solution. The gold atoms on their surfaces can be uniformly etched layer by layer, while the lateral dimensions of the gold nanoflakes remain nearly constant. The thickness of the resulting gold nanoflakes is thus determined by the etching time. Finally, the etched gold nanoflakes were cleaned with ethanol (≥99.7%) and dried with nitrogen.

TEM characterizations and FIB processing
A portion of the target gold nanoflake was transferred onto TEM grids from the original glass substrate using a fiber taper-assisted transfer method. Characterizations observed along the thickness direction were conducted inside a Thermo Scientific Talos F200X G2 TEM operated at 200 kV. An overview image of the transferred nanoflake was initially captured to carefully select multiple flat regions, from which SAED images were acquired, followed by high-resolution zoom-in images. A low beam intensity was maintained throughout the entire process to minimize possible irradiation effects on the gold nanoflake[33,34]. Subsequent post-processing (including limited background noise filtering and contrast adjustment) and data measurements were carried out using the Digital Micrograph software. The residual of the same gold nanoflake on the glass substrate was utilized to identify the thickness by means of AFM. FIB experiments were operated (Thermo Scientific, Helios G4 CX DualBeam System) to fabricate the sample used to observe the lattice structures of gold nanoflakes along the <110> beam direction. Gallium ion beam with 30 kV/0.79 nA was first used for coarse thinning of the sample to tens of micrometers. Subsequently, a lower ion beam current at 30 kV/80 pA was applied for further thinning until the sample reached a thickness of a few microns. Finally, ion beam with a rather low energy of 2 kV/39 pA was employed to gradually thin the sample to ≈100 nm.

Gold nanoflake transfer
A piece of wedge-shaped polydimethylsiloxane (PDMS) was solidified at 90 °C for 10 min on a silicon substrate with a 270 nm-thick oxidation layer to ensure a smooth subface. Firstly, one side of the subface slowly contacted the entire gold nanoflake while a small water drop was placed on the other side using a pipette, penetrating into the interfaces between PDMS, the gold nanoflake and silicon substrate during the carefully press-down process. Since the gold nanoflake was previously supported by PDMS, any probable damage of the gold nanoflake during water penetration was effectively alleviated. After complete contact, the PDMS stamp was deliberately peeled off, picking up the gold nanoflake on the PDMS. By repeating the press-down-peel-off process, gold nanoflakes can be transferred from glass substrates to

pre-patterned silicon substrates with circular holes 4 µm in diameter and 370 nm in depth.

AFM nanoindentation experiments

AFM imaging and nanoindentation measurements[36] were conducted using an Asylum Research MFP-3D AFM under ambient conditions. To prevent possible damages, the gold nanoflake to be measured was initially imaged in tapping mode at a scan rate of 0.7 Hz before the nanoindentation test. Only those gold nanoflakes without folds or bulges were selected. The nanoindentation test was performed in contact mode at a controlled displacement rate of 1 µm s^{-1} over a piezo sweep distance of 500 nm. Consecutive nanoindentation experiments with increasing applied force were executed for each sample until the final fracture. Diamond coated tips (Nanosensors, DT-NCHR) were used to mitigate wear during continuous nanoindentation experiments, whose tip radii were confirmed to be around 150 nm according to SEM images (Hitachi SU-8010). The spring constants of the cantilevers were calibrated to be 60–80 N m^{-1} using the Sader method[54], consistent with the values provided by the manufacturers. Optical sensitivity of each AFM probe in each experiment was thoroughly calibrated. The deflection of the gold nanoflake was then collected by subtracting the tip deflection from the z-piezo displacement.

DFT computations

DFT computations, as implemented in the VASP code[55,56], were performed with the PBEsol[57,58] exchange-correlation functional and the PAW[56,59] pseudopotentials. The valence-electron eigenstates were expanded using a plane wave basis set with a cutoff energy of 550 eV and were smeared using the first-order Methfessel-Paxton method with a smearing parameter of 0.2 eV. In reciprocal space, a Γ-centered Monkhorst-Pack[60] k-mesh was used with a line density ($2\pi/81$ Å^{-1}) consistent across all geometries. This k-mesh density leads, for example, to a $20 \times 20 \times 20$ mesh for gold in the 4-atom FCC unit cell and a $33 \times 33 \times 17$ mesh for gold in the 2-atom HCP unit cell, respectively. Atomic forces were relaxed to less than 0.5 meV Å^{-1} during ionic relaxations. The DFT parameters were validated in the FCC bulk structure. The computed lattice constant and elastic constants agree well with experiments, as shown in Suppl. Table 5, confirming the reliability of the DFT computations. More DFT calculations were carried out to explore the mechanism of the phase transformation in gold nanoflakes. We first considered the effect of substrate. Amorphous SiO$_2$ substrate was generated using a melt-quench approach via MD simulations with the ReaxFF force field[61]. The $2 \times 2 \times 2$ supercell was subjected to an equilibrium process at 8000 K for 175 ps, followed by a gradual cooling process to 300 K over 2 ns. The resulting amorphous structure was subsequently optimized at the DFT level.

MD simulations

To support the experimental and DFT results, we further performed MD simulations of suspended nanoindentations using the LAMMPS package. The embedded atom method (EAM) potential[53] was used to model the gold inter-atomic interactions. OVITO was used to visualize atomic configurations and analyze simulation results by identifying phase structures (common neighbor analysis) and dislocations (dislocation analysis). We modeled the indenter by using a strong repulsive potential. Each atom in the indented material interacts with the idealized indenter via the potential, $F = -K(r - R)^2$, where K is a force constant, R is the indenter radius, and r is the distance from the atom to the center of the indenter sphere. Minimum energy calculations were performed for indentations on the {0001} surface, using a repulsive potential with $A = 10.0$ eV Å^{-2} to model a spherical indenter with a 25 Å radius. The HCP gold nanoflake was represented by an 8-layer slab with a 540 Å radius containing 1015684 atoms. Periodic boundary conditions were used perpendicular to the surface, and the yellow atoms situated within ≈1 nm from the boundary were fixed, as

shown in Suppl. Fig. 17a. The indenter displacement d was changed in small steps 0.1 Å and at each step the total energy was minimized at 0 K, using a conjugate gradient algorithm.

Data availability

The data that support the findings of this study are available from the corresponding authors upon request. Source data are provided with this paper.

References

1. Li, X. Y., Wei, Y. J., Lu, L., Lu, K. & Gao, H. J. Dislocation nucleation governed softening and maximum strength in nano-twinned metals. *Nature* **464**, 877–880 (2010).
2. Wu, G., Chan, K. C., Zhu, L. L., Sun, L. G. & Lu, J. Dual-phase nanostructuring as a route to high-strength magnesium alloys. *Nature* **545**, 80–83 (2017).
3. Cheng, Z., Zhou, H. F., Lu, Q. H., Gao, H. J. & Lu, L. Extra strengthening and work hardening in gradient nanotwinned metals. *Science* **362**, eaau1925 (2018).
4. Lu, Y., Song, J., Huang, J. Y. & Lou, J. Fracture of sub-20nm ultrathin gold nanowires. *Adv. Funct. Mater.* **21**, 3982–3989 (2011).
5. Deng, C. & Sansoz, F. Near-ideal strength in gold nanowires achieved through microstructural design. *ACS Nano* **3**, 3001–3008 (2009).
6. Lu, L., Shen, Y. F., Chen, X. H., Qian, L. H. & Lu, K. Ultrahigh strength and high electrical conductivity in copper. *Science* **304**, 422–426 (2004).
7. Zhu, T. & Li, J. Ultra-strength materials. *Prog. Mater. Sci.* **55**, 710–757 (2010).
8. Richter, G. et al. Ultrahigh strength single crystalline nanowhiskers grown by physical vapor deposition. *Nano Lett.* **9**, 3048–3052 (2009).
9. Yu, Q., Qi, L., Mishra, R. K., Li, J. & Minor, A. M. Reducing deformation anisotropy to achieve ultrahigh strength and ductility in Mg at the nanoscale. *Proc. Natl. Acad. Sci. USA.* **110**, 13289–13293 (2013).
10. Wu, Z. X., Ahmad, R., Yin, B. L., Sandlobes, S. & Curtin, W. A. Mechanistic origin and prediction of enhanced ductility in magnesium alloys. *Science* **359**, 447–451 (2018).
11. Ritchie, R. O. The conflicts between strength and toughness. *Nat. Mater.* **10**, 817–822 (2011).
12. Zhang, Z. J. et al. Dislocation mechanisms and 3D twin architectures generate exceptional strength-ductility-toughness combination in CrCoNi medium-entropy alloy. *Nat. Commun.* **8**, 14390 (2017).
13. Zhu, Y. T. & Liao, X. Z. Nanostructured metals - Retaining ductility. *Nat. Mater.* **3**, 351–352 (2004).
14. Wu, G. et al. Hierarchical nanostructured aluminum alloy with ultrahigh strength and large plasticity. *Nat. Commun.* **10**, 8 (2019).
15. Uchic, M. D., Dimiduk, D. M., Florando, J. N. & Nix, W. D. Sample dimensions influence strength and crystal plasticity. *Science* **305**, 986–989 (2004).
16. Li, X. Y., Lu, L., Li, J. G., Zhang, X. & Gao, H. J. Mechanical properties and deformation mechanisms of gradient nanostructured metals and alloys. *Nat. Rev. Mater.* **5**, 706–723 (2020).
17. Chen, Y. et al. Phase engineering of nanomaterials. *Nat. Rev. Chem.* **4**, 243–256 (2020).
18. Kou, H. N., Lu, J. & Li, Y. High-strength and high-ductility nanostructured and amorphous metallic materials. *Adv. Mater.* **26**, 5518–5524 (2014).
19. Wang, J. W. et al. In situ atomic-scale observation of twinning-dominated deformation in nanoscale body-centred cubic tungsten. *Nat. Mater.* **14**, 594–600 (2015).
20. Sedlmayr, A. et al. Existence of two twinning-mediated plastic deformation modes in Au nanowhiskers. *Acta Mater.* **60**, 3985–3993 (2012).

21. Cao, G. et al. Superplasticity in gold nanowires through the operation of multiple slip systems. *Adv. Funct. Mater.* **28**, 8 (2018).

22. Seo, J. H. et al. Superplastic deformation of defect-free Au nanowires via coherent twin propagation. *Nano Lett.* **11**, 3499–3502 (2011).

23. Kim, J. H. et al. Tensile testing of ultra-thin films on water surface. *Nat. Commun.* **4**, 6 (2013).

24. Gall, K., Diao, J. K. & Dunn, M. L. The strength of gold nanowires. *Nano Lett.* **4**, 2431–2436 (2004).

25. Lagos, M. J., Sato, F., Galvao, D. S. & Ugarte, D. Mechanical deformation of nanoscale metal rods: when size and shape matter. *Phys. Rev. Lett.* **106**, 4 (2011).

26. Yu, Q. et al. Strong, ductile, and tough nanocrystal-assembled freestanding gold nanosheets. *Nano Lett.* **22**, 822–829 (2022).

27. Wang, J. W. et al. Near-ideal theoretical strength in gold nanowires containing angstrom scale twins. *Nat. Commun.* **4**, 1742 (2013).

28. Wang, Y. M. et al. Controlling factors in tensile deformation of nanocrystalline cobalt and nickel. *Phys. Rev. B* **85**, 014101 (2012).

29. Zhang, B. et al. Enhanced mechanical properties in β-Ti alloy aged from recrystallized ultrafine β grains. *Mater. Des.* **195**, 109017 (2020).

30. Huang, X. et al. Synthesis of hexagonal close-packed gold nanostructures. *Nat. Commun.* **2**, 292 (2011).

31. Liu, L. F. et al. Atomically smooth single-crystalline platform for low-loss plasmonic nanocavities. *Nano Lett.* **22**, 1786–1794 (2022).

32. Pan, C. X. Y. et al. Large area single crystal gold of single nanometer thickness for nanophotonics. *Nat. Commun.* **15**, 2840 (2024).

33. Lee, S. B., Jung, J. & Han, H. N. Transition to body-centered cubic structure in Au thin films under electron-beam irradiation. *Acta Mater.* **247**, 9 (2023).

34. Zhu, Q. et al. Free-standing two-dimensional gold membranes produced by extreme mechanical thinning. *ACS Nano* **14**, 17091–17099 (2020).

35. Cowley, J. M. et al. Electron diffraction and electron microscopy in structure determination. *Int. Tables Crystallogr.* **B**, 297–402 (2010).

36. Lee, C., Wei, X., Kysar, J. W. & Hone, J. Measurement of the elastic properties and intrinsic strength of monolayer graphene. *Science* **321**, 385–388 (2008).

37. Komaragiri, U. & Begley, M. R. The mechanical response of free-standing circular elastic films under point and pressure loads. *J. Appl. Mech.* **72**, 203–212 (2005).

38. Bhatia, N. M. & Nachbar, W. Finite indentation of an elastic membrane by a spherical indenter. *Int. J. Non Linear Mech.* **3**, 307–324 (1968).

39. Zheng, S., Shinzato, S., Ogata, S. & Mao, S. X. Experimental molecular dynamics for individual atomic-scale plastic events in nanoscale crystals. *J. Mech. Phys. Solids* **158**, 104687 (2022).

40. Zheng, H. et al. Discrete plasticity in sub–10-nm-sized gold crystals. *Nat. Commun.* **1**, 144 (2010).

41. Greer, J. R. & Nix, W. D. Nanoscale gold pillars strengthened through dislocation starvation. *Phys. Rev. B* **73**, 245410 (2006).

42. Krebs, J. et al. Cast aluminium single crystals cross the threshold from bulk to size-dependent stochastic plasticity. *Nat. Mater.* **16**, 730–736 (2017).

43. Niu, M. et al. Precipitate evolution and strengthening behavior during aging process in a 2.5 GPa grade maraging steel. *Acta Mater.* **179**, 296–307 (2019).

44. Shiroka, T. Introduction to solid state physics. *Contemp. Phys.* **61**, 221–222 (2020).

45. Guo, G. Y. & Wang, H. H. Calculated elastic constants and electronic and magnetic properties of bcc, fcc, and hcp Cr crystals and thin films. *Phys. Rev. B* **62**, 5136–5143 (2000).

46. Kohn, W. & Sham, L. J. Self-consistent equations including exchange and correlation effects. *Phys. Rev.* **140**, A1133–A1138 (1965).

47. Tran, R. et al. Surface energies of elemental crystals. *Sci. Data* **3**, 160080 (2016).

48. Wang, C. et al. Generalized-stacking-fault energy and twin-boundary energy of hexagonal close-packed Au: a first-principles calculation. *Sci. Rep.* **5**, 10213 (2015).

49. Li, P. et al. Thermal effect and rayleigh instability of ultrathin 4H hexagonal gold nanoribbons. *Matter* **2**, 658–665 (2020).

50. Cheng, H., Yang, N., Lu, Q., Zhang, Z. & Zhang, H. Syntheses and properties of metal nanomaterials with novel crystal phases. *Adv. Mater.* **30**, 1707189 (2018).

51. Fan, Z. et al. Surface modification-induced phase transformation of hexagonal close-packed gold square sheets. *Nat. Commun.* **6**, 6571 (2015).

52. Li, Q. et al. Pressure-induced phase engineering of gold nanostructures. *J. Am. Chem. Soc.* **140**, 15783–15790 (2018).

53. Foiles, S. M., Baskes, M. I. & Daw, M. S. Embedded-atom-method functions for the fcc metals Cu, Ag, Au, Ni, Pd, Pt, and their alloys. *Phys. Rev. B* **33**, 7983–7991 (1986).

54. Sader, J. E. et al. Spring constant calibration of atomic force microscope cantilevers of arbitrary shape. *Rev. Sci. Instrum.* **83**, 103705 (2012).

55. Kresse, G. & Furthmüller, J. Efficient iterative schemes for ab initio total-energy calculations using a plane-wave basis set. *Phys. Rev. B* **54**, 11169–11186 (1996).

56. Kresse, G. & Joubert, D. From ultrasoft pseudopotentials to the projector augmented-wave method. *Phys. Rev. B* **59**, 1758–1775 (1999).

57. Perdew, J. P., Burke, K. & Ernzerhof, M. Generalized gradient approximation made simple. *Phys. Rev. Lett.* **78**, 1396–1396 (1997).

58. Perdew, J. P. et al. Restoring the density-gradient expansion for exchange in solids and surfaces. *Phys. Rev. Lett.* **100**, 136406 (2008).

59. Blöchl, P. E. Projector augmented-wave method. *Phys. Rev. B* **50**, 17953–17979 (1994).

60. Monkhorst, H. J. & Pack, J. D. Special points for Brillouin-zone integrations. *Phys. Rev. B* **13**, 5188–5192 (1976).

61. Hühn, C., Wondraczek, L. & Sierka, M. Dynamics of ultrathin gold layers on vitreous silica probed by density functional theory. *Phys. Chem. Chem. Phys.* **17**, 27488–27495 (2015).

62. Zhu, W. et al. A novel high-strength β-Ti alloy with hierarchical distribution of α-phase: The superior combination of strength and ductility. *Mater. Des.* **168**, 107640 (2019).

63. Chong, Y., Bhattacharjee, T., Yi, J., Shibata, A. & Tsuji, N. Mechanical properties of fully martensite microstructure in Ti-6Al-4V alloy transformed from refined beta grains obtained by rapid heat treatment (RHT). *Scr. Mater.* **138**, 66–70 (2017).

64. Wan, Y. et al. Bulk nanocrystalline high-strength magnesium alloys prepared via rotary swaging. *Acta Mater.* **200**, 274–286 (2020).

65. Bian, M. Z. et al. A heat-treatable Mg–Al–Ca–Mn–Zn sheet alloy with good room temperature formability. *Scr. Mater.* **138**, 151–155 (2017).

66. Jian, W. W. et al. Ultrastrong Mg alloy via nano-spaced stacking faults. *Mater. Res. Lett.* **1**, 61–66 (2013).

67. Ravi Kiran, U. et al. Refractory metal alloying: A new method for improving mechanical properties of tungsten heavy alloys. *J. Alloys Compd.* **709**, 609–619 (2017).

68. Ren, C. et al. Methods for improving ductility of tungsten - A review. *Int. J. Refract. Hard Met.* **75**, 170–183 (2018).

69. Li, T. et al. Ultra-strong tungsten refractory high-entropy alloy via stepwise controllable coherent nanoprecipitations. *Nat. Commun.* **14**, 3006 (2023).

70. Ditta, A., Wei, L., Xu, Y. & Wu, S. Effect of hot extrusion and optimal solution treatment on microstructure and properties of spray-formed Al-11.3Zn-2.65Mg-1Cu alloy. *J. Alloys Compd.* **797**, 558–565 (2019).

71. Zhao, Y. H., Liao, X. Z., Cheng, S., Ma, E. & Zhu, Y. T. Simultaneously increasing the ductility and strength of nanostructured alloys. *Adv. Mater.* **18**, 2280–2283 (2006).
72. Liddicoat, P. V. et al. Nanostructural hierarchy increases the strength of aluminium alloys. *Nat. Commun.* **1**, 63 (2010).
73. Çavuşoğlu, O. et al. Microstructural features and mechanical properties of 22MnB5 hot stamping steel in different heat treatment conditions. *J. Mater. Res. Technol.* **9**, 10901–10908 (2020).
74. Li, Y. et al. Ductile 2-GPa steels with hierarchical substructure. *Science* **379**, 168–173 (2023).
75. Wang, W. et al. Effects of Cr and Zr additions on microstructure and properties of Cu-Ni-Si alloys. *Mater. Sci. Eng. A* **673**, 378–390 (2016).
76. Huang, L. et al. Effect of trace alloying elements on the stress relaxation properties of high strength Cu–Ti alloys. *Mater. Sci. Eng. A* **846**, 143281 (2022).
77. Krasilnikov, N., Lojkowski, W., Pakiela, Z. & Valiev, R. Tensile strength and ductility of ultra-fine-grained nickel processed by severe plastic deformation. *Mater. Sci. Eng. A* **397**, 330–337 (2005).
78. Zhao, Y. et al. High tensile ductility and strength in bulk nanostructured nickel. *Adv. Mater.* **20**, 3028–3033 (2008).
79. Wu, X. et al. Nanodomained nickel unite nanocrystal strength with coarse-grain ductility. *Sci. Rep.* **5**, 11728 (2015).
80. Karimpoor, A. A., Erb, U., Aust, K. T. & Palumbo, G. High strength nanocrystalline cobalt with high tensile ductility. *Scr. Mater.* **49**, 651–656 (2003).
81. Ahmed, R., de Villiers Lovelock, H. L., Davies, S. & Faisal, N. H. Influence of Re-HIPing on the structure–property relationships of cobalt-based alloys. *Tribol. Int.* **57**, 8–21 (2013).

Acknowledgements

Author contributions

T.Z. performed HRTEM, FIB, mechanical experiments, data analysis and transferred samples. Y.T. and C.P. fabricated samples and contributed to the sample transfer. X.W. contributed to the mechanical experiments. J.P., T.L. and B.Y. developed the theory and performed the DFT calculations and MD simulations. W.Y., Y.G., B.Y., P.W., and L.T. conceived the work. All authors have contributed to the writing of this article.

Competing interests

The authors declare no competing interests.

Additional information

Supplementary information The online version contains supplementary material available at https://doi.org/10.1038/s41467-025-56047-x.

Correspondence and requests for materials should be addressed to Binglun Yin, Pan Wang or Yang Gao.

Peer review information *Nature Communications* thanks Gunther Richter and the other, anonymous, reviewer(s) for their contribution to the peer review of this work. A peer review file is available.

Reprints and permissions information is available at http://www.nature.com/reprints

Publisher's note Springer Nature remains neutral with regard to jurisdictional claims in published maps and institutional affiliations.